Influence of cohesive clay on wave–current ripple dynamics captured in a 3D phase diagram

Xuxu Wu[1,2], Jonathan Malarkey[3], Roberto Fernández[4], Jaco H. Baas[3], Ellen Pollard[1], and Daniel Parsons[5]

[1]Energy and Environment Institute, University of Hull, Hull, HU6 7RX, UK.
[2]School of Environmental Sciences, University of Hull, Hull, HU6 7RX, UK.
[3]School of Ocean Sciences, Bangor University, Menai Bridge, LL59 5AB, Wales, U.K.
[4]Department of Civil and Environmental Engineering, The Pennsylvania State University, State College, PA 16802, USA.
[5]Loughborough University, Loughborough, LE11 3TU, U.K.

Correspondence to: Xuxu Wu (x.wu@hull.ac.uk)

Abstract. Wave–current ripples that develop on seabeds of mixed non-cohesive sand and cohesive clay are commonplace in coastal and estuarine environments. While laboratory research on ripples forming in these types of mixed-bed environments is relatively limited, it has identified deep cleaning, the removal of clay below the ripple troughs, as an important factor controlling ripple development. New large-scale flume experiments seek to address this sparsity in data by considering two wave-current conditions with initial clay content, C_0, ranging from 0 to 18.3%. The experiments record ripple development and pre- and post-experiment bed clay contents, to quantify clay winnowing. The present experiments are combined with previous wave–only, wave–current and current–only experiments to produce a consistent picture of larger and smaller flatter ripples over a range of wave-current conditions and C_0. Specifically, the results reveal a sudden decrease in the ripple steepness for $C_0 > 10.6\%$, likely associated with a three-orders of magnitude decrease in hydraulic conductivity. Accompanying the sudden change in steepness is a gradual linear decrease in wavelength with C_0 for $C_0 > 7.4\%$. Ultimately, for the highest values of C_0, the bed remains flat, but clay winnowing still takes place, albeit at a rate two orders of magnitude lower than for rippled beds. For a given flow, the initiation time, when ripples first appear on a flat bed, increases with increasing C_0. This, together with the fact that the bed remains flat for the highest values of C_0, demonstrates that the threshold of motion increases with C_0. The inferred threshold enhancement, and the occurrence of large and small ripples, is used to construct a new three-dimensional phase diagram of bed

characteristics involving the wave and current Shields parameters and C_0, which has important implications for morphodynamic modelling.

1 Introduction

In coastal and estuarine environments, the superposition of waves and currents, termed combined wave–current flows, is a common occurrence. In these environments, which include continental shelves, the shoreface, and tidal flats, combined wave–current flows frequently form ripples on the seabed (e.g., Osborne and Greenwood, 1993; Li and Amos, 1999; Héquette et al., 2008; Gao, 2019). Ripple dynamics play a crucial role in sediment transport, which in turn affects the predictions of large-scale coastal morphodynamic numerical models (Brakenhoff et al., 2020), the underwater scour around civil engineering structures (Sumer et al., 2001), and the transport of nutrients and contaminants (Vercruysse et al., 2017). Moreover, combined-flow ripples have been found in the geological record, thus providing key information for reconstructing paleoenvironments (e.g., Myrow et al., 2006, Beard et al., 2017). It is therefore crucial to examine how combined-flow hydrodynamics control ripple dimensions and vice versa, particularly in muddy coastal and estuarine environments that are widespread in nature (Healy et al., 2002) and characterised by sediment consisting of a mixture of cohesive clay and non-cohesive sand. A full understanding of this process will ultimately prove significant for coastal and estuarine management and ecological balance maintenance, especially as such areas may face more extreme weather events in the context of climate change and sea level rise (e.g., Mousavi et al., 2011, Vitousek et al., 2017).

To date, however, there has been a scarcity of relevant literature on this topic. Wu et al. (2022) were the first to consider ripple dynamics in sand–clay mixtures under combined flows. Their study showed that small flat ripples formed for initial clay contents, C_0, greater than 10.6% under hydrodynamic conditions that formed large equilibrium ripples in clean sand. Moreover, Wu et al. (2022) demonstrated that clay winnowing efficiency plays a significant role in the development towards clean-sand-like ripples on mixed sand–clay beds. They also highlighted the process of deep cleaning of clay below ripple troughs for $C_0 \leq 10.6\%$, whereas Wu et al. (2018) revealed a more modest deep accumulation of clay beneath rippled beds under wave-alone conditions for $C_0 \leq 7.4\%$. This suggests a dynamic balance between loss

and accumulation of clay during ripple development. However, the key factors governing this dynamic balance, and the resulting ripple size, remain unclear, primarily due to the limited number of flow conditions considered thus far. This knowledge deficiency in mixed sand–clay experiments is reflected in the existing ripple predictors, i.e., bedform phase diagrams and empirical formulae, that are based exclusively on clean-sand experiments.

Phase diagrams group similar bedform types and cross-sectional geometries for known hydrodynamic conditions and sediment properties (e.g., Van den Berg and Van Gelder, 1993). In the last thirty years, a substantial number of experimental studies has made progress in compiling combined-flow ripple phase diagrams (Arnott and Southard, 1990, Kleinhans, 2005, Dumas et al., 2005, Cummings et al., 2009, Perillo et al., 2014). Using a range of combined-flow conditions in an experimental flume, Perillo et al. (2014) expanded the bedform phase diagrams of Arnott and Southard (1990) and Dumas et al. (2005) by subdividing bedform types based on planform geometry. Baas et al.'s (2021) phase diagram, based on field observations of bedforms on an intertidal flat in the Dee Estuary, U.K., captured bedform types generated under a wider range of flow conditions, including those generated under waves and currents at angles to one another. Compared to wave-alone and current-alone ripple predictors, relatively few predictors are available for combined flow ripples. Tanaka and Dang (1996) modified a widely used predictor for wave ripples developed by Wiberg and Harris (1994) by considering the influence of grain size and the relative strength of the wave and current velocities on the ripple size. Khelifa and Ouellet (2000) developed a new formulation to predict ripple dimensions by introducing an effective combined-flow mobility parameter.

The experiments of Wu et al. (2022) were conducted under a single wave-dominated combined-flow condition, but further study considering wider hydrodynamic conditions is required for a more comprehensive understanding of the interaction between ripple development and winnowing-induced clay loss from beds. These insights are critical for the development of morphodynamic models applicable in muddy estuaries and the coastal zone. Therefore, the present study extends Wu et al.'s (2022) experiments and describes a systematically collected set of data from large-scale flume experiments on ripple development. This study also draws in available sand–clay experiments under current-alone and wave-alone conditions (Baas et al., 2013; Wu et al., 2018). The three specific objectives of this study

were: (1) to compare ripple development and occurrence on beds with similar initial clay contents under different hydrodynamic conditions; (2) to compare clay winnowing efficiency during ripple development, under different flow conditions; and (3) to propose a new phase diagram for bedforms generated in sand–clay substrates to systematise the experiments, using the knowledge gained from objectives 1 and 2.

2 Materials and Methods

2.1 Experiment setup

The experiments were undertaken in a recirculating flume tank in the Total Environment Simulator at the University of Hull. Three equal-size channels, 11 m long and 1.6 m wide, were separated by brick walls, 0.2 m high, in the tank (Figure 1). Combined flow conditions were maintained during the experiments and flow velocities in each channel were measured by a 25 Hz Vectrino profiler throughout the entire duration of the experiments. Freshwater was used in all experiments, and the water depth, h, was set to 0.4 m. A 2-MHz ultrasonic ranging sensor (URS), containing 32 probes, monitored the ripple evolution and migration in the test section (Figure 1). Further details of the instrument setup are available from Wu et al. (2022).
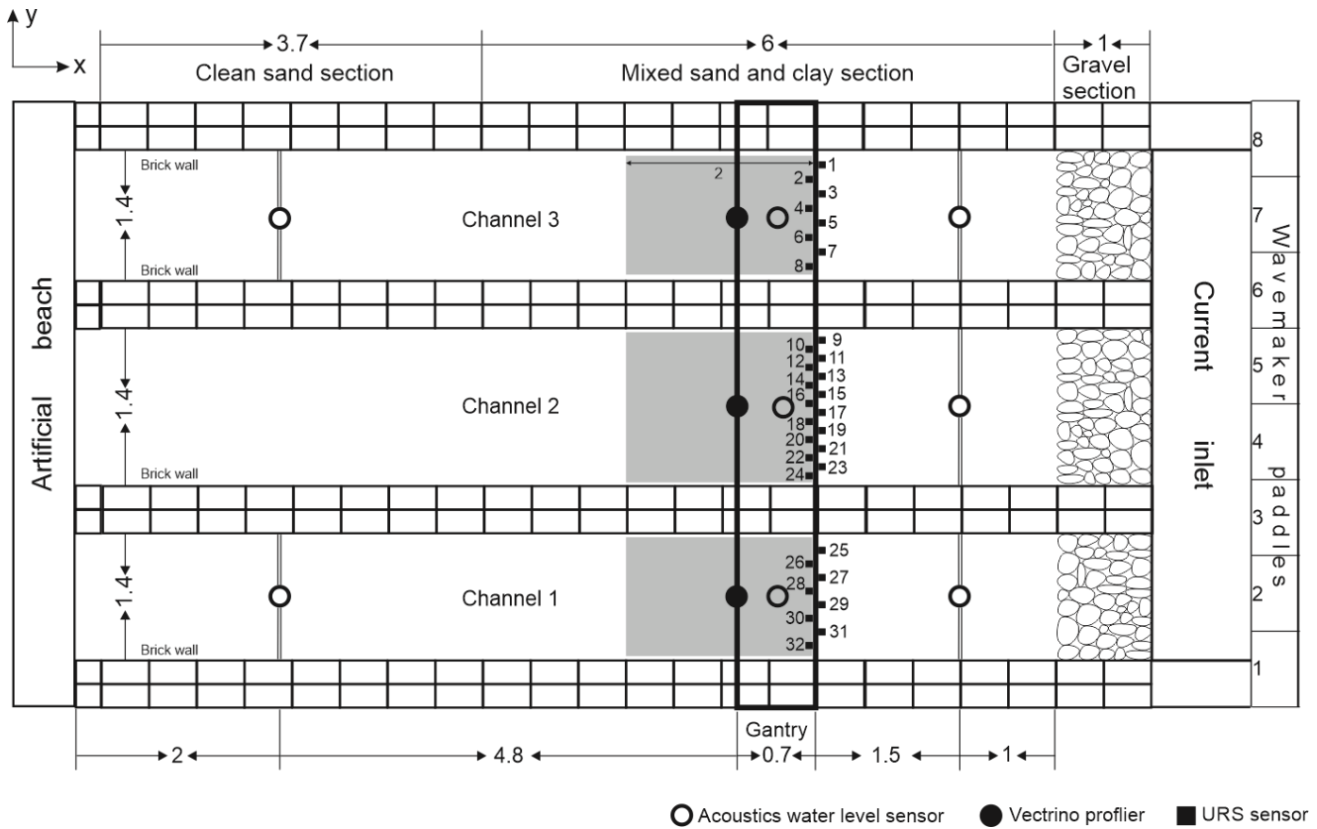
Figure 1.   Plan view of the experimental setup. The grey area was scanned by an Ultrasonic Range System (URS) with numbered sensors (black squares). White and black circles denote acoustic water level sensors and Vectrino profilers, respectively. Dimensions are in metres.

2.2 Experimental procedure and wave–current settings

To complement Wu et al.'s (2022) wave-dominated flow condition, with depth-average current, $U_c \approx 0.16$ m s^{-1}, and wave velocity amplitude, $U_w \approx 0.32$ m s^{-1}, (Table A1), the present experiments comprised two additional flow conditions of increased relative current strength, with $U_c \approx 0.3$ m s^{-1} and $U_w \approx 0.27$ and 0.13 m s^{-1}, with wave heights, H, of 0.05 and 0.1 m, and wave period, T, of 2 s (Table 1). The wave–current flow conditions (WC1, in Table A1 from Wu et al., 2022; WC2 and WC3, in Table 1) are numbered according to increasing relative current strength, from the weakest, WC1, to the strongest, WC3. The experiments involved different initial mass concentrations of clay, C_0, in each of the three channels, with the same flow conditions for each channel. The bed was composed of a well-sorted sand

with a median diameter, D_{50}, of 0.45 mm and cohesive kaolinite clay with $D_{50} = 0.0089$ mm. The sand, clay, water depth and wave period in the present experiments were the same as in Wu et al. (2022). The order of the experiments was from high to low clay content, by taking advantage of the natural winnowing of the bed during the experiments. Run 1, the sand-only control, and Run 2, with C_0 of 9.9%, 13.1%, and 18.3% by dry weight in channels 1 to 3, were under WC3 flow conditions (Table 1). The beds in Run 2 remained essentially flat after 650 min. In Run 3, the wave height was doubled (WC2) and the duration was increased to 1850 min. In Run 4, three beds were prepared with relatively low clay contents, $C_0 \leq$ 6.4%, and the same WC3 conditions as in Runs 1 and 2 were imposed.

To ensure homogeneity in the mixed section of each channel (Figure 1), the clay was mixed into the sand using a handheld plasterer's mixer and the sediment beds were flattened using a wooden leveller between runs. A terrestrial 3D laser scanner (FARO Focus3D X330) was used to scan the sediment bed in each channel before and after the run, after the water had been drained. Furthermore, the flow was temporarily stopped during the runs at pre-set times to make URS bed scans and collect sediment cores from the bed using syringes with a diameter of 20 mm and a maximum length of 90 mm. These short pauses in the experiments resulted in negligible bed deposition of suspended clay particles due to their slow settling velocity. Details of the protocols for URS bed scanning and sediment core collection are available from Wu et al. (2022). Channel 2 of Run 4 was excluded from the analysis, because core samples collected from the flat bed showed that the sediment in this channel was not sufficiently well mixed.

Wu et al. (2022) justified their choice of flow conditions by demonstrating that they were largely consistent with the observations of Baas et al.'s (2021) intertidal field site in the macrotidal Dee Estuary (U.K.), where $D_{50} = 0.227$ mm, $0 < h \leq 3.5$ m, $0 < U_c \leq 0.6$ m/s, $0 < U_w \leq 0.45$ m/s and $0 < C_0 \leq 14\%$. Baas et al. (2021) produced a phase diagram based on the equivalent wave-only and current-only skin friction, τ_w and τ_c, using Malarkey and Davies' (2012) shear stress calculation with the strong non-linear option. Here in Figure 2, Baas et al.'s (2021) phase diagram has been non-dimensionalised to the equivalent wave-only and current-only Shields parameters, θ_w and θ_c, given by $\tau/(\rho_s - \rho)gD_{50}$, where ρ_s is the sediment density (= 2650 kg m^{-3}), ρ is the water density (= 1000 kg m^{-3} for freshwater, 1027 kg m^{-3} for seawater) and g is the acceleration due to gravity (= 9.81 m s^{-2}). This allows the present experiments (Table 1, WC2 and WC3) and previous wave–current experiments (WC1, Table A1), together with the

current-alone and wave-alone experiments of Baas et al. (2013) and Wu et al. (2018) (Tables A2 and A3),

to be compared to one another. In Figure 2, the critical Shields parameter for the clean-sand threshold of

motion, θ_0, is determined with Soulsby's (1997) formula, $\theta_0 = 0.3/(1+1.2D_*) + 0.055[1–\exp(–0.02D_*)]$,

where $D_* = D_{50}[(\rho_s–\rho)g\nu^2/\rho]^{1/3}$ and ν is the kinematic viscosity of water. It should be noted that the

threshold of motion is different for each grain size: $\theta_0 = 0.032$ for WC1-WC3, $D_{50} = 0.45$ mm, and Wu et

al. (2018), $D_{50} = 0.496$ mm; $\theta_0 = 0.061$ for Baas et al. (2013), $D_{50} = 0.143$ mm; and $\theta_0 = 0.05$ for Baas et

al. (2021), $D_{50} = 0.227$ mm. In Figure 2 the threshold of motion appears as a straight line given by $\theta_w+\theta_c$

= θ_0 because, unlike in the field study of Baas et al. (2021), all experimental flows were co-linear. Whilst

θ_0 is clearly affected by grain size, it is assumed that the other boundaries in the phase diagram are not.

The phase diagram (Figure 2) identifies the flow conditions of Wu et al. (2018) and WC1 as wave-

dominated (W), $\theta_c < 0.2\theta_w$, those of Baas et al. (2013) as current-dominated (C), $\theta_c > 3.3\theta_w$ and those of

the present experiments (WC2 and WC3) as wave-current (WC), $0.2\theta_w < \theta_c < 3.3\theta_w$. Whilst not all

experiments produced ripples (open circles and NR in Table 1), all the data were between the washout

limit $\theta_w+\theta_c = 0.18$ and the clean-sand threshold of motion, $\theta_w+\theta_c = \theta_0$. It is anticipated that ultimately

above washout there are flat featureless upper stage plane beds (for waves and currents at angles this may

be complicated by the occurrence of lunate ripples, Baas et al., 2021). The reason that not all conditions

produce ripples is related to higher clay contents enhancing the threshold shear stress. This is a

shortcoming of the phase diagram of Baas et al. (2021) and is the justification for the new phase diagram

proposed in this paper.

Table 1 Experimental parameters

Run/ Channel	Flow code[1]	Duration (min)	C_0 (%)	H (m)	U_w (m s^{-1})	U_c (m s^{-1})	θ_w	θ_c	Bed description[2]
1/2	WC3	600	0	0.05	0.14	0.31	0.047	0.031	R
2/1	WC3	650	9.9	0.05	0.13	0.31	0.042	0.031	NR
2/2	WC3	650	13.1	0.05	0.14	0.29	0.047	0.027	NR
2/3	WC3	650	18.3	0.05	0.13	0.31	0.042	0.031	NR
3/1	WC2	1850	8.4	0.1	0.27	0.32	0.124	0.033	R
3/2	WC2	1850	10.8	0.1	0.27	0.30	0.124	0.029	R

3/3	WC2	1850	16.3	0.1	0.27	0.31	0.124	0.031	NR
4/1	WC3	1250	2.5	0.05	0.13	0.25	0.042	0.020	R
4/3	WC3	1250	6.4	0.05	0.12	0.29	0.037	0.027	R

[1]The flow code represents the relative current strength, where WC1 (Wu et al., 2022, Table A1) is the weakest and WC3 is the strongest. For WC1 conditions (Table A1), corresponding to $0 \leq C_0 \leq 12.6$, $0.31 \leq U_w \leq 0.33$ m/s, $0.15 \leq U_c \leq 0.2$ m/s, $0.15 \leq \theta_w \leq 0.16$ and $0.007 \leq \theta_c \leq 0.13$, ripples always developed.

[2]R - ripples formed and NR - no ripple formed.

2.3 Data processing

Raw bed elevation profiles recorded from each URS scan, consisting of 16 profiles for channel 2 and 8 profiles for channels 1 and 3, were processed after de-spiking and smoothing. A Matlab 'peaks and troughs' tool was used to identify individual ripple heights, η, and wavelengths, λ, followed by calculation of the mean across-channel values of λ_t and η_t at a bed scanning time of t to construct the development curves of ripple height and wavelength and hence determine equilibrium bedform dimensions. Following Wu et al. (2022), the equilibrium ripple height, η_e, and wavelength, λ_e, and equilibrium time for ripple height, T_η, and wavelength, T_λ, were calculated using the procedure of Baas et al. (2013), which includes a delay time for the first appearance of ripples, t_i, and an initial wavelength, λ_i:

$$\frac{\eta_t}{\eta_e} = 1 - 0.1^{\frac{t-t_i}{T_\eta - t_i}}, \tag{1}$$

$$\frac{\lambda_t - \lambda_i}{\lambda_e - \lambda_i} = 1 - 0.1^{\frac{t-t_i}{T_\lambda - t_i}}. \tag{2}$$

The ripples were also characterised by their steepness, RS, and ripple symmetry index, RSI, given by

$$RS = \eta_e / \lambda_e, \tag{3}$$

$$RSI = \lambda_s / \lambda_l, \tag{4}$$

where λ_s and λ_l are the length of the stoss and lee side of the ripple (RSI < 1.3 for symmetric and 1.3 < RSI < 1.5 for quasi-asymmetric ripples, Perillio et al., 2014) (Table 2).

Sediment cores from the initial flat bed and the ripple crests and troughs were sliced into 10-mm intervals for grain-size analysis using a Malvern Mastersizer 2000. In the crest cores. the region corresponding to

the active layer (ripple crest down to trough) were sliced into 5-mm intervals for better resolution of the clay content within the ripples. The measured clay content, C, in the sediment cores was further processed to acquire the total amount of clay removed from the bed, I, by integrating the clay deficit, defined as C_{def} = C_0–C, from the lowest reference level, $z = -100$ mm up to the crest level, $z = 0$ mm. These quantities allow the equivalent clean-sand depth, d_c, to be given by

$$d_c = I/C_0, \qquad\qquad (5)$$

which is the amount of clean sand available in the uppermost layers for ripple growth. Finally, the sediment concentration profiles were characterised by a Gaussian-type function. Full details of all data processing are available from Wu et al. (2022).
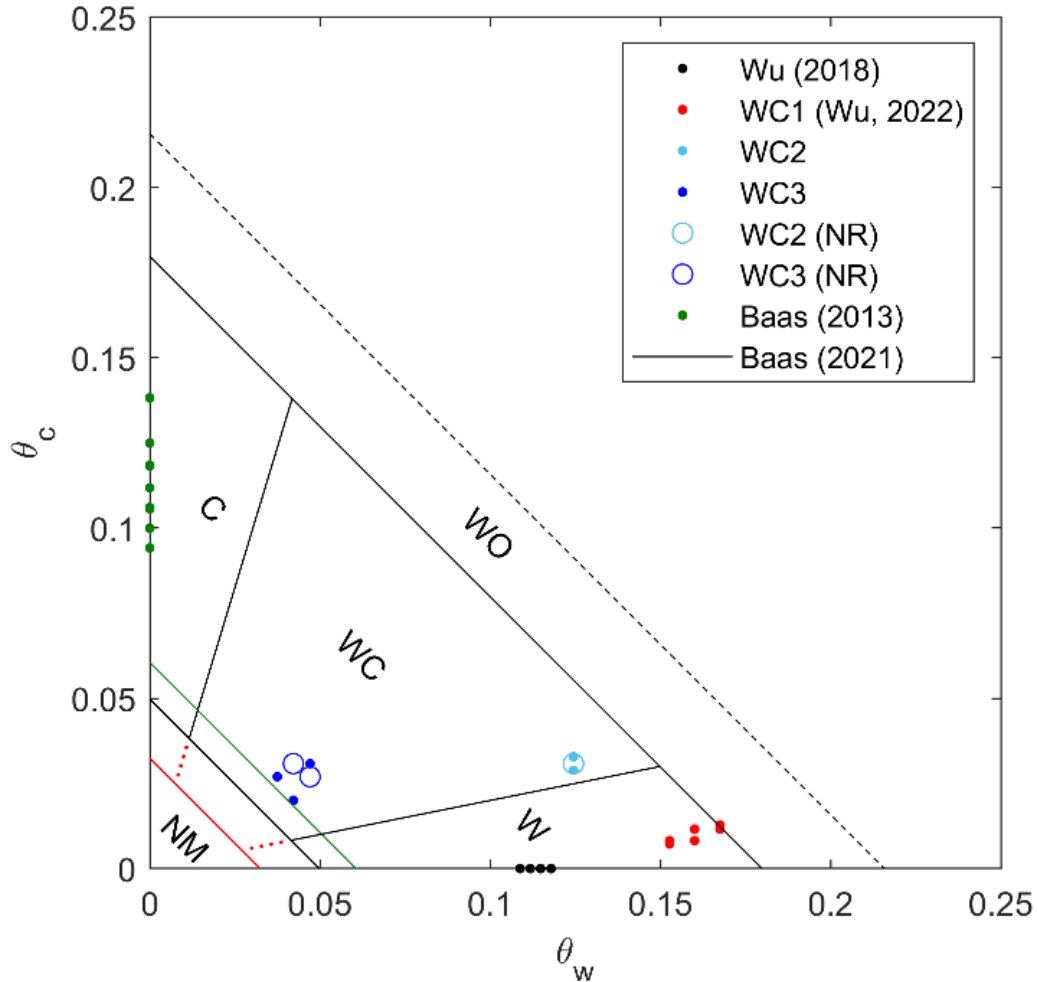
 Figure 2. Non-dimensional, θ_w-θ_c phase diagram after Baas et al. (2021), showing all wave-only (Wu et al., 2018), wave-current, WC1 (Wu et al., 2022), WC2 and WC3, and current-only (Baas et al., 2013) conditions. Open circles show cases where no ripples (NR) were present, and the various regions are marked C - current-dominant, WC - wave-current, W - wave-dominant, NM - no motion and WO - washout. The additional threshold of motion lines, θ_0, are coloured red for WC1-WC3 and Wu et al. (2018) and green for Baas et al. (2013).

3. Results

3.1 Ripple development

Figure 3 shows the development of ripple height and wavelength for different C_0-values in the present experiments (WC2 and WC3). For $C_0 = 0\%$ (WC3), clean-sand ripples appeared immediately after the start of the experiment ($t_i = 0$), developed rapidly and reached an equilibrium height, $\eta_e = 15.5$ mm, and wavelength, $\lambda_e = 147.9$ mm (Figure 3a and b; Table 2). As shown in Figure 4a, the clean-sand ripples were two-dimensional in plan view, with straight continuous crestlines. In cross-section, these ripples were quasi-asymmetric, with a ripple symmetry index (RSI) of 1.4 and a ripple steepness (RS) of 0.11 (Table 2).

2..
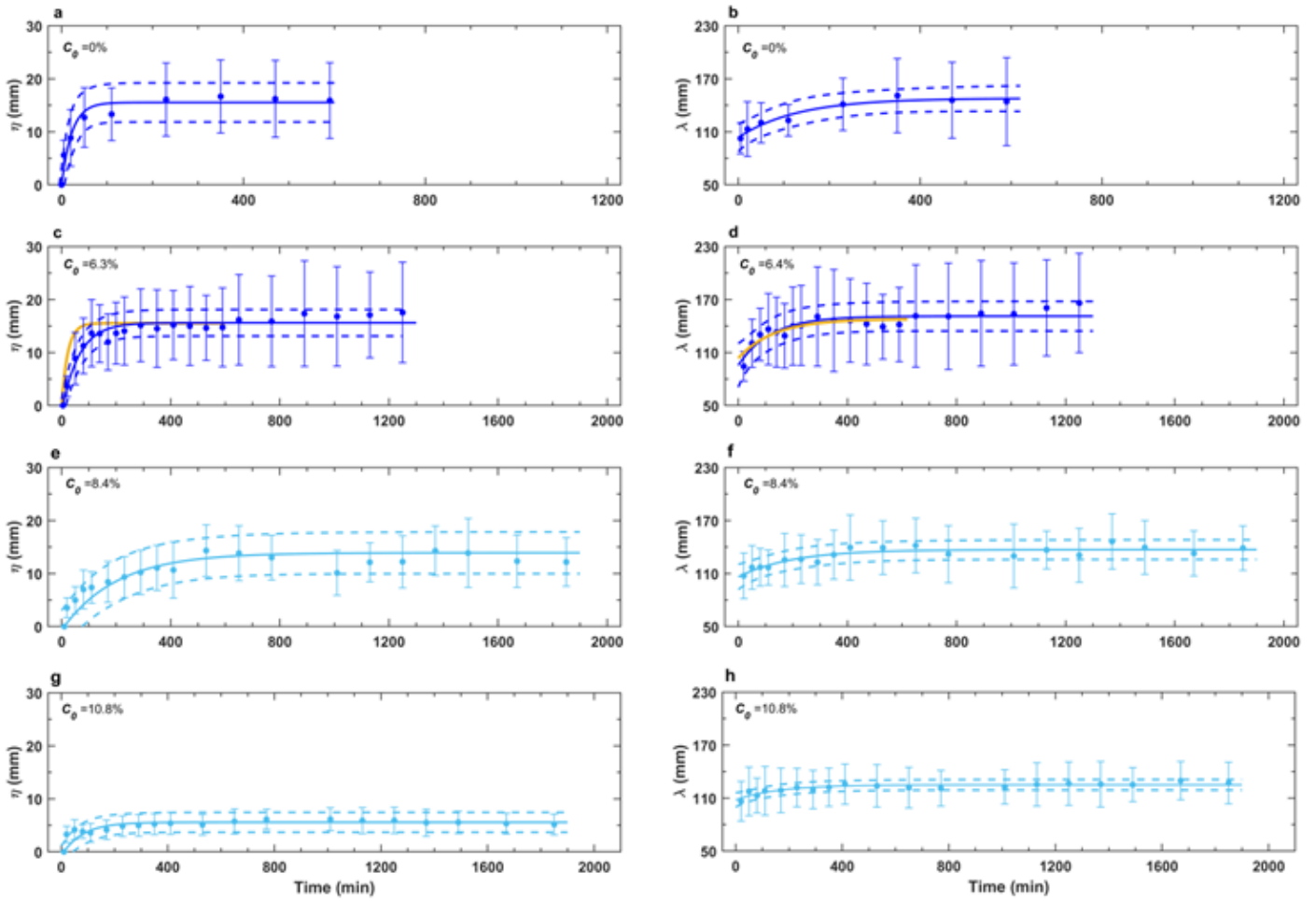
Figure 3. Development of ripple height and wavelength for WC3 (dark blue dots in a – d) and WC2 (light blue dots in e - f) for different values of C_0. The error bars denote one standard deviation from the mean dimension. Continuous dark and light blue lines are based on fitting to Equations 1 and 2, and dashed dark and light blue lines are their corresponding 95% confidence intervals. The yellow lines in c and d are the best-fit curves for clean sand from a and b.

205
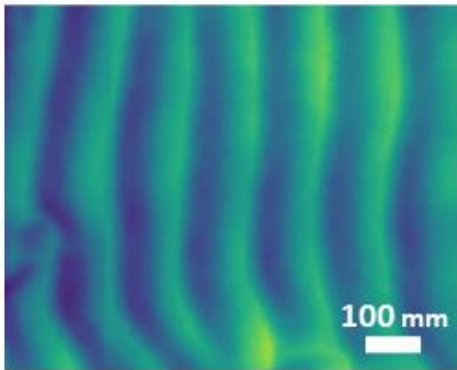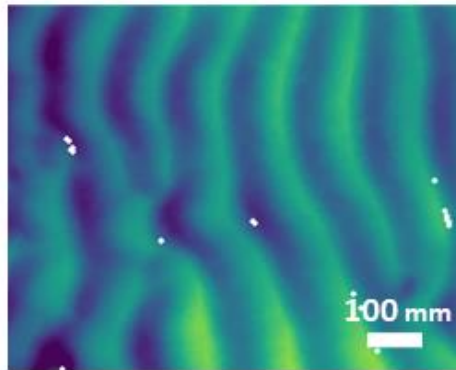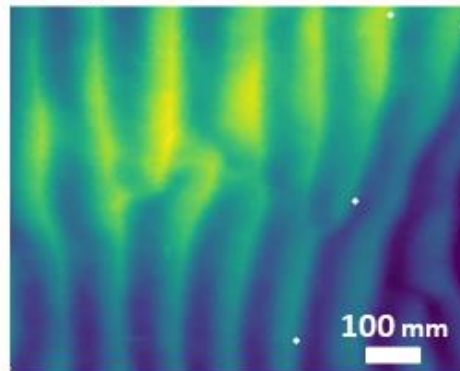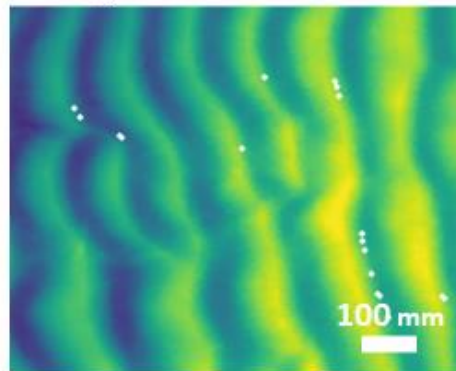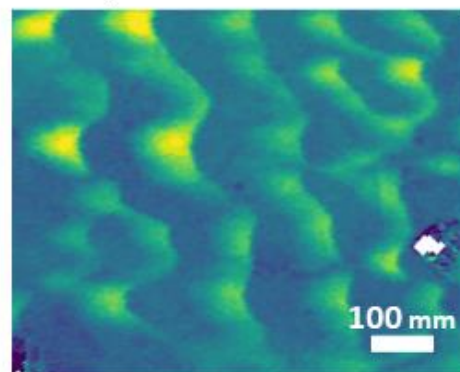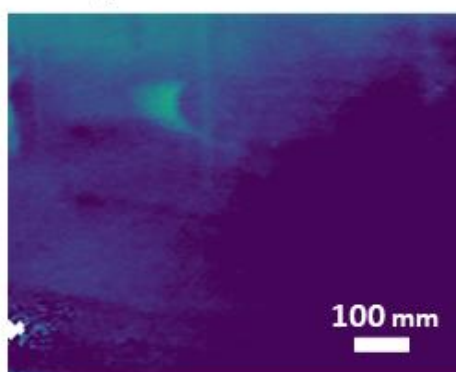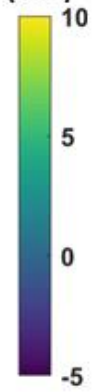
Figure 4. Plan view of ripple morphology in the test section acquired by the 3D FARO scanner at the end of the experiment. a – c: rippled beds formed under WC3 conditions; d – f: bed states under WC2 conditions. C_0 is the initial clay content and the flow direction is from left to right. Note the elevation scale for d also applies to a – c, and elevation scale for f also applies to e.

210

For C_0 = 2.5 and 6.4% (WC3), the ripples developed to similar equilibrium dimensions as their clean-sand counterparts, η_e = 15.6 mm and λ_e = 152.5 mm for C_0 = 6.4% (Figure 3c and d), and the bed was again covered in two-dimensional, quasi-asymmetric ripples (Figure 4b and c).

The three WC3 cases with $C_0 \geq 9.9\%$ remained flat over the entire ten-hour duration (Table 2), implying there was no sand movement in these cases. Despite flat-bed conditions persisting, winnowing during the experiment caused the bed clay content to decrease, as will be seen in the next section, such that the initial clay contents were C_0 = 8.4, 10.8 and 16.3% for the three channels in the subsequent run under WC2 conditions, where U_w was doubled to 0.27 m s^{-1}. For C_0 = 8.4% (WC2), small ripples appeared at t = 10 min. Thereafter, ripple dimensions developed gradually over a period of around seven hours, stabilising to an equilibrium height and wavelength of 13.9 and 137 mm (Figure 3e and f). The equilibrium ripples retained similar geometries to those developed under WC2 conditions, characterised by two-dimensional plan forms with quasi-asymmetric cross sections (Table 2; Figure 4d).

At C_0 = 10.8% (WC2), ripples again appeared at t = 10 min, but only grew to equilibrium dimensions of η_e = 5.6 mm and λ_e = 125 mm (Figure 3g and h, Table 2). These small ripples were three-dimensional with discontinuous, sinuous crestlines in plan view. In cross-section, these ripples were asymmetric and flatter, with RSI = 1.6 and RS = 0.04 (Figure 4e, Table 2). The general trends in equilibrium time for ripple height, T_η, and wavelength, T_λ, with C_0 were similar to those found by Wu et al. (2022). For the C_0 = 16.3% (WC2) case, the bed remained flat (Figure 4f); there was no sand movement.

229 Table 2. Bedform characteristics

Flow ID	C_0 (%)	Bedform type	η_e (mm)	T_η (min)	R^2	λ_e (mm)	λ_i (mm)	T_λ (min)	R^2	t_i (min)	RSI	RS
WC3	0	QAR	15.5 ± 1.5	53	0.95	147.9 ± 9.4	103.5 ± 10.2	302	0.95	0	1.5 ± 0.4	0.11 ± 0.03
WC3	2.5	QAR	14.8 ± 0.68	71	0.91	144.8 ± 5.5	99.1 ± 11.7	330	0.8	0	1.5 ± 0.5	0.11 ± 0.04
WC3	6.4	QAR	15.6 ± 0.67	151	0.94	152 ± 5.9	105 ± 14.8	344	0.79	5	1.5 ± 0.4	0.1 ± 0.04
WC3	9.9	NR	–	–	–	–	–	–	–	–	–	–
WC3	13.1	NR	–	–	–	–	–	–	–	–	–	–
WC3	18.3	NR	–	–	–	–	–	–	–	–	–	–
WC2	8.4	QAR	13.9 ± 1.29	471	0.80	137 ± 3.7	107.7 ± 8.6	465	0.79	10	1.4 ± 0.4	0.09 ± 0.03
WC2	10.8	AR	5.6 ± 0.2	273	0.96	125 ± 1.9	108.9 ± 5	377	0.79	10	1.6 ± 0.5	0.04 ± 0.01
WC2	16.3	NR	–	–	–	–	–	–	–	–	–	–

230 QAR: Quasi-Asymmetric Ripple

231 AR: Asymmetric Ripple

232 NR: No Ripples

233 R^2: Squared correlation coefficient of the best fit curve

234 ±: Standard deviation

3.2 Comparison of pre- and post-experiment vertical bed clay content

Figure 5 shows the pre- and post-experiment, vertical clay content in the bed, based on grain-size analysis of the sediment cores. In each case, the vertical grey solid and dashed lines show the value of $C_0 \pm$ one standard deviation. Figure 5a–d show the pre-experiment clay contents and Figure 5e–h show the post-experiment clay contents for WC3. The three WC3 flat-bed cases (Figure 5f–h) were used as the pre-experiment cores for WC2, with post-experiment cores shown in Figure 5i–k. For WC3, $C_0 = 6.4\%$, the sediment cores show a 100% clay loss in the active layer (ripple crest down to the ripple trough level) and an additional layer of substantial clay loss with a thickness of c. 80 mm below the active layer (Figure 5e). The equivalent clean-sand depth (black horizontal dashed line), $d_c = I/C_0$, was 57 mm, more than two times the ripple height (25 mm). For WC2, $C_0 = 8.4\%$ (Figure 5i), a small amount of clay, 2.9%, remained at the base of the active layer. In contrast to the $C_0 = 6.4\%$ case, $d_c = 13.1$ mm is smaller than the ripple height (17.5 mm). For $C_0 = 10.8\%$ (Figure 5j), there were much smaller ripples (Figure 3g and h, and Table 2), which contained a higher clay content of 8% at the base of the active layer. Here, $d_c = 10.1$ mm, compared to the ripple height of 5.6 mm.

No ripples formed for $C_0 \geq 9.9\%$ under WC3 conditions and $C_0 = 16.3\%$ under WC2 conditions (Table 2). Nevertheless, the post-experiment sediment cores clearly demonstrate clay loss at all measured depths (Figure 5 f–h, and k). Specifically, there was an approximate 10% reduction in clay content on beds with $C_0 = 16.3\%$ and 18.3%, whereas there was a higher percentage of clay loss from the lower C_0 beds: 15% for $C_0 = 9.9\%$ and 18% for $C_0 = 13.1\%$. This difference is reflected in the d_c values: 15 and 19 mm for $C_0 = 9.9\%$ and 13.1% compared to 14 and 11 mm for $C_0 = 16.3\%$ and 18.3%.
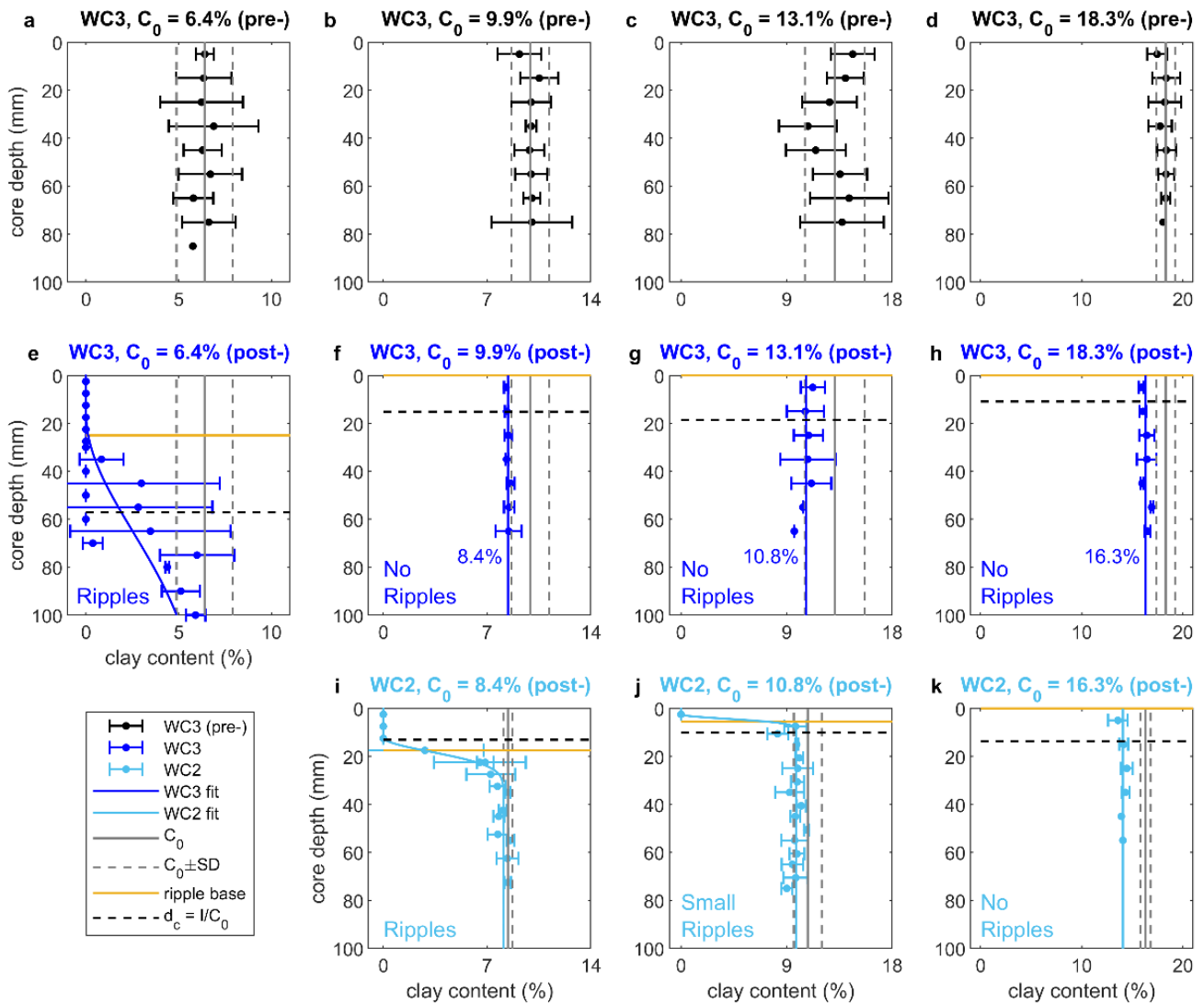
255

Figure 5. Pre-and post-experiment vertical profiles of clay content in cores collected from beds in the mixed sand–clay section. In each case, the pre- and post-experiment profiles are directly above one another: for WC3 conditions (pre- a–d and post- e–h) and for WC2 conditions (pre- f–h and post- i– k). Note the three WC3 flat-bed cases (f–h) were used as the pre-experiment cores for WC2 (i–k).

260   The dark/light blue solid lines are the fits to WC3/WC2 post-experiment clay contents at each depth. The grey vertical solid and dashed lines represent mean initial clay content, C_0, and one standard deviation from the mean for comparison. The horizontal error bars denote one standard deviation of

the mean clay content at that depth. For post-experiment cores, the yellow lines represent the ripple base and the dashed horizontal black lines represent the equivalent clean-sand depth.

4 Discussion

4.1 The effect of clay and hydrodynamic conditions on ripple dimensions and geometries

Wu et al.'s (2022) experiments, under WC1 flow conditions, revealed two distinct types of equilibrium ripples with a threshold C_0 value of 10.6%. For $C_0 \leq 10.6\%$, large 2D ripples with similar dimensions and geometries to their clean-sand counterparts developed, whereas for $C_0 > 10.6\%$ only small flat 3D ripples developed. In the present experiments under WC2 conditions, this discontinuity in equilibrium ripple size was also observed (Table 2), with small equilibrium ripples generated in the $C_0 = 10.8\%$ case, consistent with $C_0 > 10.6\%$. Additionally, the clay content at the base of the active layer was c. 8%, which is consistent with Wu et al.'s (2022) threshold that restricts the ripples from growing beyond their small, flat stage. Wu et al. (2022) argued that this latter 8% threshold was more general than the $C_0 = 10.6\%$ threshold as it was found to be also the case at the base of the active layer for Baas et al.'s (2013) $C_0 = 13\%$ threshold for fine-sand current ripple sizes (Table A2).

Figure 6a, which includes WC1-WC3 and Wu et al.'s (2018) wave-only cases, shows that the two ripple types correspond to two quite distinct constant steepness groupings, RS, which change at $C_0 = 10.6\%$. For WC3 conditions, the $C_0 = 10.6\%$ small–large ripple threshold is hypothetical as the bed shear stresses for what would be small ripples are below the threshold of motion for $C_0 \geq 9.9\%$, hence no ripples form (RS = 0). The threshold of motion will be discussed in Section 4.3. Figure 6a demonstrates another feature of the larger wave-only and wave–current ripples which can also be seen in the data of Perillo et al. (2014). The steepness is directly related to the current shear stress: RS = 0.145 for Wu et al. (2018), where $\theta_c = 0$; RS = 0.120 for WC1, where $\theta_c = 0.008$-0.013 and RS = 0.103 for WC2 and WC3, where $\theta_c = 0.020$-0.033 (Tables 1, A1 and A3, and Figure 2). This is the background current shear stress limiting the growth of wave ripples with increasing effect, such that for the strongest current the steepness is only just above the threshold for boundary-layer separation and vortex ejection (RS > 0.1, Sleath, 1984). Compared to

the large ripples, the steepness of the small ripples was 0.04, implying there was no boundary layer separation (Figure 6a and Wu et al., 2022).

290 Other than this reduction in steepness, current strength was found to have a modest influence on ripple geometry; for example, RSI ≈ 1.5 for the large ripples for WC2 and WC3 (Table 2), compared to RSI ≈ 1.4 for WC1 (Wu et al., 2022). However, previous flume experiments with an increasing current component have shown a more dramatic effect (Yokokawa, 1995, Dumas et al., 2005, Perillo et al., 2014). Perillo et al. (2014) found that ripples became more asymmetric, with RSI increasing from 1.4 to 1.7, as

295 U_c increased from 0.1 to 0.3 m s^{-1}, with $U_w = 0.25$ m s^{-1}. The relatively coarse sediment used in WC1-WC3, $D_{50} = 0.45$ mm, may have resulted in a greater tendency towards 2D symmetric ripples, compared to Perillo et al.'s (2014) finer sediment, $D_{50} = 0.25$ mm, forming more 3D asymmetric ripples (Cummings et al., 2009, Pedocchi and García, 2009).

Figure 6b shows that the non-dimensional equilibrium wavelength, λ_e/D_{50}, is approximately constant for

300 $C_0 \leq 7.4\%$. However, unlike the ripple steepness, there is a gradual linear reduction with C_0 for $C_0 > 7.4\%$ (the upper limit of Wu et al.'s (2018) experiments). Interestingly, this 7.4% limit is very similar to the 8% limit at the base of the active layer discussed above. Based on the trend lines fitted to the data in Figure 6b, the clean-sand equivalent equilibrium ripple wavelengths fall into two distinct groups: a wave-dominant group, comprising the WC1 and Wu et al. (2018) cases where $\lambda_e/D_{50} = 278$, and a wave-current

305 group, comprising the WC2 and WC3 cases where $\lambda_e/D_{50} = 329$ (18% larger). All ripples with $C_0 \leq 10.6\%$ are clearly 2D and orbital in nature (Figure 4a–d; Figure 3a–d in Wu et al., 2022 and Wu et al., 2018), including such characteristic features as bifurcations (Perron et al., 2018), implying that the wavelength is directly proportional to the wave orbital diameter. This together with the fact that skin friction stresses show that the flow can reverse ($\theta_w > \theta_c$), even for WC3 conditions, implies that the wavelength should be

310 described by $\lambda_e = \alpha d_{wc}$, where α is the constant of proportionality (= 0.62, according to Wiberg and Harris, 1994) and d_{wc} is the orbital diameter enhanced by the current. The orbital diameter scales the ripple spacing, as it represents the distance a neutrally buoyant particle can move in half a wave cycle (Clifton and Dingler, 1984). With the addition of a current, this particle can move further and Appendix B explains how d_{wc} is determined based on a sinusoidal wave. The value of d_{wc} is open to some interpretation, as the

315 near-bed wave orbital diameter is combined with the depth-averaged current. Here, it has been chosen to

reflect the difference in the clean-sand values of λ_e/D_{50} between the two groups: $d_{wc}/D_{50} = 469$ and 539, for the wave-dominant and wave-current groups, respectively. Wiberg and Harris' (1994) definition confirms that these flows are both within the orbital ripple regime ($d_{wc}/D_{50} \leq 1754$).

With the wave-current orbital diameter, d_{wc}, now determined it is possible to calculate the quantity α (= λ_e/d_{wc}), which is shown in Figure 6c. While there is scatter ($R^2 = 0.762$), all the data collapses onto a single curve with a similar behaviour to the wavelength (Figure 6b):

$$\alpha = \begin{cases} 0.61, & C_0 \leq C_{0m}, \\ 0.61 - 3.36(C_0 - C_{0m}), & C_0 > C_{0m}, \end{cases} \qquad (6)$$

where $C_{0m} = 7.4\%$, such that $\alpha = 0.31$ when $C_0 = 16.3\%$. For $C_0 \leq 7.4\%$, ripples are orbital (α is constant), and the constant is very close to Wiberg and Harris' (1994) clean-sand value, 0.62. For $C_0 > 7.4\%$, where α reduces, the ripples effectively become increasingly anorbital in character.
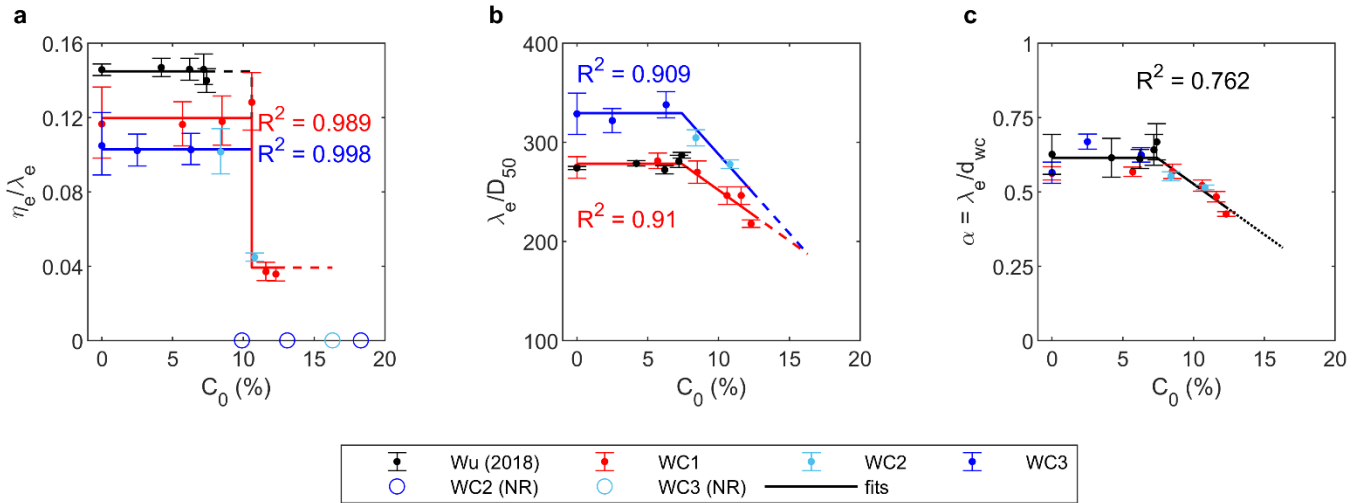
Figure 6. Equilibrium ripple steepness, $RS = \eta_e/\lambda_e$, (a), non-dimensional ripple wavelength, λ_e/D_{50}, (b) and the α parameter, $\alpha = \lambda_e/d_{wc}$, (c) as a function of initial bed clay content, C_0, for Wu et al. (2018) and WC1-WC3. Open circles show that no ripples (NR) were present and dots are based on measured values of η_e, λ_e and α and their error bars. Solid lines correspond to least-square-fits to the data with R^2-values quoted.

4.2 Potential factors controlling deep cleaning of clay

Winnowing is an important mechanism in ripple development, because it provides the necessary supply of clean sand in the active layer from which ripples can grow. Significant clay loss beneath equilibrium ripples was observed in the $C_0 = 6.4\%$ (WC3) case (Figure 5e), as occurred for $C_0 \leq 10.6\%$ in WC1 (Wu et al., 2022). Wu et al. (2022) highlighted the process of deep cleaning of clay from the substrate after ripples reached equilibrium, with clay loss occurring in a layer approximately three to four times the ripple height below the equilibrium ripple base. However, the deep-cleaning effect was considerably weaker in the $C_0 = 8.4\%$ (WC2) case, despite the increased hydrodynamic forcing compared to WC3 (Figure 5i). In Figure 7, clay loss is quantified by the average mass flux of clay out of the bed over each experiment, F_b, given by I/t_d, where t_d is the duration of the experiment, allowing the rippled- and flat-bed cases to be compared with one another. For large ripples, $F_b \approx 3.5 \times 10^{-6}$ g mm^{-2} min^{-1} under WC1 and WC3 conditions, whereas it decreased to 9.4×10^{-7} g mm^{-2} min^{-1} under WC2 conditions. By comparing ripple migration to pore water velocity magnitude, Wu et al. (2022) demonstrated winnowing dominance over hyporheic processes for WC1. While winnowing dominance is undoubtedly also the case for WC2 and WC3 in the active layer (Figure 5e and i), it is not necessarily the case below the active layer. In fact ripple migration rates were faster for WC2 conditions, $23 - 34$ mm min^{-1}, than for WC1 and WC3 conditions, $5 - 20$ and $8 - 13$ mm min^{-1}, respectively. For N$_2$O cycling beneath current ripples, Jiang et al. (2022) showed that increasing ripple migration can result in directional changes of hyporheic pore water flow in the bed from vertical to horizontal, potentially inhibiting clay removal or in the extreme case trapping the clay at depth. In the $C_0 = 8.4\%$ case, c. 20% of the clay was still able to be removed from a thin layer of approximately 20 mm beneath the active layer (Figure 5i); suggesting that pore water direction did not change completely from vertical to horizontal. F_b decreased to c. 8.5×10^{-7} g mm^{-2} min^{-1} for small ripples under WC1 and WC2 conditions, which is comparable to the large ripple flux for WC2. This suggests strong bed cohesion, as well as ripple migration, controls clay winnowing at depth (Teitelbaum et al., 2021; 2022). Further study is needed to quantify the relationship between ripple migration and clay winnowing efficiency.

A similar difference in deep cleaning between WC2 and WC3 was observed in the cases where no ripples formed (NR): $F_b = 4.8 \times 10^{-8}$ g mm^{-2} min^{-1} for WC3 and $F_b = 1.9 \times 10^{-8}$ g mm^{-2} min^{-1} for WC2. For flat

beds, Higashino et al. (2009) found that increasing the shear velocity, u_*, increases the pore water velocity, but decreases its penetration depth. If u_* is proportional to $\theta_{rms}^{1/2} = (\frac{1}{2}\theta_w^2 + \theta_c^2)^{1/4}$, where θ_{rms} is the root-mean-square of the instantaneous shear stress, then u_* is 50% larger for WC2 than for WC3, suggesting that the ability of WC2 conditions to remove clay at depth is reduced. Compared to rippled beds, the fluxes from flat beds are two orders of magnitude smaller; this is consistent with previous studies showing that hyporheic exchange is enhanced by the presence of bedforms (Huettel et al., 1996; Packman et al., 2004; Higashino et al., 2009). Furthermore, Figure 7 shows the general stepping down of the flux as C_0 increases; this is probably an indication of the clay forming blocked layers as can occur in sand-silt mixtures (e.g., Bartzke et al., 2013) which reduces permeability and also hydraulic conductivity, thus inhibiting the clay's removal.

Ignoring changes in porosity and cohesion, the hydraulic conductivity is approximately proportional to D_{10m}^2, where D_{10m} is the 10th percentile of the sand–clay mixture (Chapuis, 2012). For the mixture, there is little overlap in the sand and clay size distributions, $D_{50} \gg D_{50c}$, where D_{50c} is the median diameter of the clay particles (~ 0.009 mm) and $D_{10} = 0.34, 0.3$ and 0.072 mm for the sand in the Wu et al. (2018), WC1-3 and Baas et al. (2013) cases. As C_0 increases, D_{10m}, and therefore the conductivity, will decrease gradually. However, when $C_0 \geq 10\%$, D_{10m} switches from its approximate clean-sand value (~ D_{10}) to a much smaller size associated with the clay (~ D_{50c}), resulting in a 3-orders of magnitude reduction for the Wu et al. (2018) and WC1-3 cases and a 2-orders of magnitude reduction for Baas et al. (2013). This reduction in hydraulic conductivity alone, does not fully explain the behaviour seen in Figure 7, as there are the effects of changes in permeability and erosion threshold to consider as well. However, it may be the reason for the drastic change in ripple steepness at $C_0 = 10.6\%$, for the Wu et al. (2018) and WC1-3

380 cases (Figure 6a), and at the slightly higher value of $C_0 = 13\%$, for the Baas et al. (2013) cases, discussed in Section 4.1.
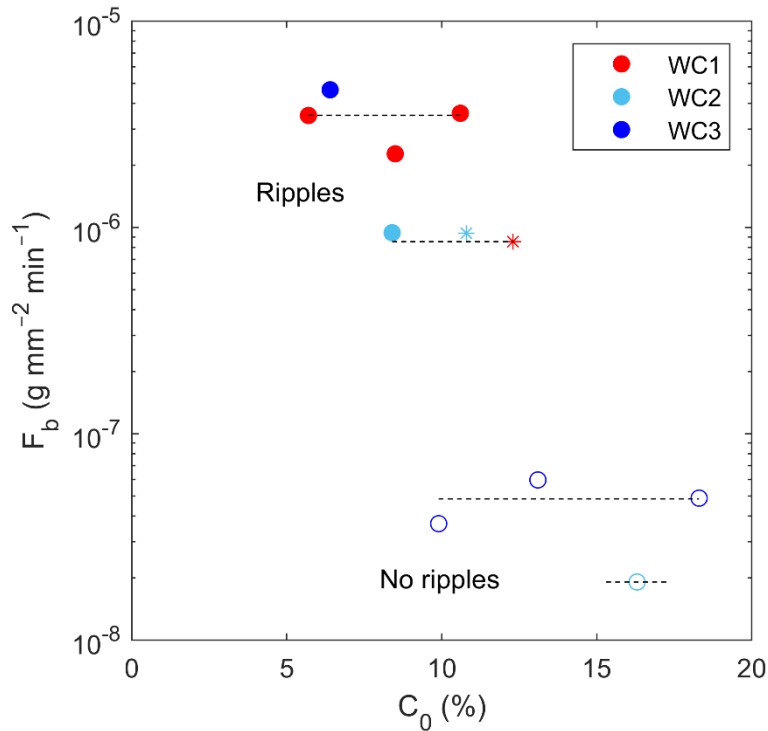
Figure 7.   Average clay mass flux out of the bed, F_b, against initial clay content, C_0, for WC1 (red; Wu et al., 2022), WC2 (light blue) and WC3 (dark blue). Here solid circles, asterisks and open circles signify large, small and no ripples.

4.3 Enhanced threshold of motion

The phase diagram of Figure 2 shows several cases without ripples (NR) (cf. Figure 6a and Table 2), despite the skin friction being above the clean-sand threshold of motion ($C_0 \geq 16.3\%$ for WC2 and $C_0 \geq$ 9.9% for WC3). The explanation for this discrepancy is that the clean-sand threshold of motion is
390 enhanced by the presence of the clay. According to Whitehouse et al. (2000), for $C_0 \leq 30\%$ the enhanced threshold of motion can be expressed generically as

$$\theta_{0E} = \theta_0(1 + P_\theta C_0), \qquad (7)$$

where P_θ is usually taken to be 20, but it can be anywhere in the range $6.7 \le P_\theta \le 45$. For WC1-WC3 and Wu et al. (2018), where $D_{50} = 0.45$ and 0.496 mm, respectively, the clean-sand threshold is $\theta_0 = 0.032$. For combined colinear wave–current flow, the threshold line is described by $\theta_{0E} = \theta_w + \theta_c$, where $\theta_c + \theta_w$ is the maximum stress in the wave cycle. This results in the threshold line in Figure 2 moving diagonally upward towards the upper right-hand corner with increasing C_0. If θ_{0E} for WC1-WC3 and Wu et al. (2018) is to be consistent with the bed characterisations (Tables 1, A1 and A3), it is necessary for $\theta_{0E} < \theta_w + \theta_c$, when ripples are present (R), and $\theta_{0E} > \theta_w + \theta_c$, when ripples are absent (NR). With $P_\theta = 20$, for WC3 and $C_0 \ge 9.9\%$, $\theta_{0E} \ge 0.095 > \theta_w + \theta_c$, which is consistent with the R/NR bed characterisations. However, for WC2 and $C_0 = 16.3\%$, $\theta_{0E} = 0.136 < \theta_w + \theta_c$, which is inconsistent with its NR characterisation (Table 1). Taking $C_0 = 16.3\%$ (WC2) as the limiting case, $\theta_{0E} = \theta_w + \theta_c = 0.155$, this gives a higher P_θ of 23 in Equation 7 which restores consistency and is still within Whitehouse et al.'s (2000) range. Figure 8a–f shows the magnitude of the time-varying skin friction using

$$\theta = |\theta_w \cos\sigma t + \theta_c|, \tag{8}$$

where $\sigma = 2\pi/T$ and the values of θ_w and θ_c are obtained from Tables 1, A1 and A3, compared with θ_{0E} using Equation 7 with $P_\theta = 23$ (yellow line). For all wave-only and wave-current cases, the above threshold (rippled-bed) and below threshold (flat-bed) cases are grouped together. Figure 8g shows the initiation time, t_i, when ripples begin to develop, from Tables 2, A1 and A3. In all cases, the skin friction is above threshold for only a fraction of the wave cycle. For each hydrodynamic condition, as the threshold increases with increasing C_0, these wave-cycle fractions above threshold decrease, with a corresponding increase in t_i (Figure 8g), until the flat-bed cases, where the skin friction is always below threshold (Figure 8e and f). In each below-threshold case there is an additional dashed line, which corresponds to the threshold based on the clay content at the end of the experiments (Figure 5f, g, h and k). Apart from WC2 and $C_0 = 16.3\%$, which is just above threshold at the end of the experiment (Figure 8f), and WC3 and $C_0 = 6.4\%$, which is just below threshold, by about the same amount (Figure 8a), this new enhancement ($P_\theta = 23$ in Equation 7) is consistent with all combined wave-current and wave-only cases (Tables 1, A1 and A3).
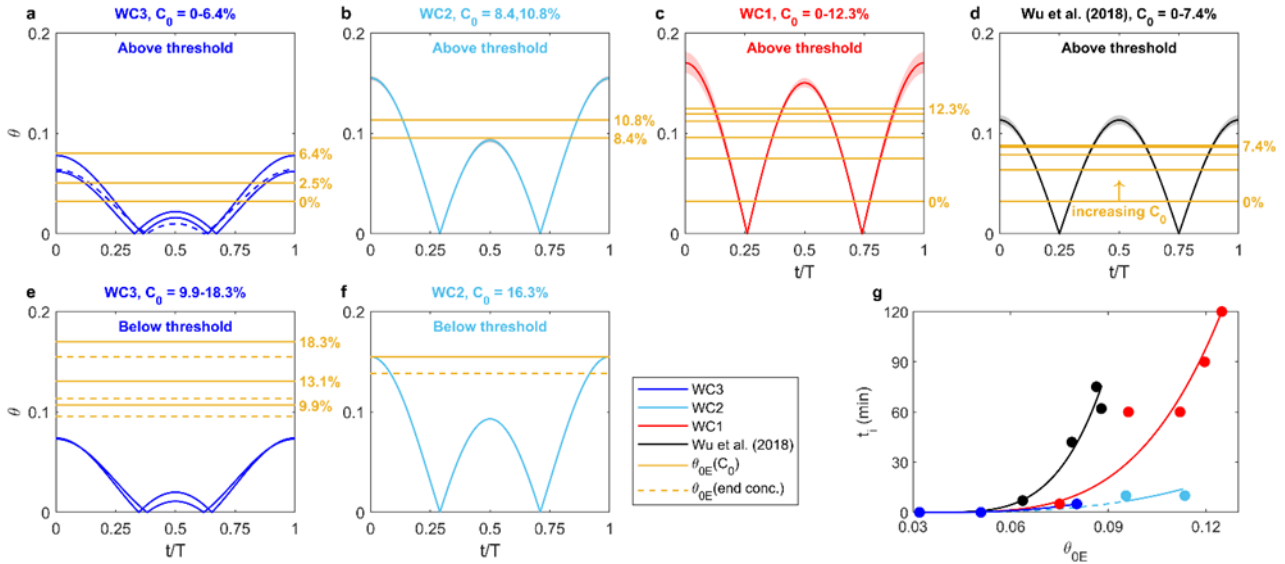
Figure 8. Time-varying skin friction using Equation 8 compared to θ_{0E} using Equation 7 with $P_\theta = 23$, for the above- and below-threshold WC3 cases (a, e) and WC2 cases (b, f) and the above-threshold WC1 cases (c) and Wu et al. (2018) wave-only cases (d); and the initiation time, t_i, versus θ_{0E} (g), grouped according to flow condition. The legend applies to all panels. In (a) the dashed blue line corresponds to the $C_0 = 6.4\%$ case; in (c, d) the shaded region corresponds to the range of instantaneous skin friction values and in (e, f) the below threshold cases show an additional dashed line for θ_{0E} corresponding to the final sediment concentration.

In Baas et al.'s (2013) fine-sand, current-only experiments (Table A2), runs with $C_0 \geq 5.4\%$ were below the enhanced threshold, $\theta_c < \theta_{0E}$, based on Equation 7 with $P_\theta = 20$. This is inconsistent with the observations, as ripples appeared in these runs, indicating that this enhancement is too strong for $D_{50} = 0.143$ mm. Baas et al. (2019) found a far more modest threshold enhancement of $P_\theta = 3$ in their threshold experiments for a similar grain size ($D_{50} = 0.142$ mm), where the velocity was stepped up sequentially over mixtures of sand and kaolinite clay until motion was detected. However, Baas et al.'s (2019) enhancement is a conservative estimate, since there was likely a cumulative effect of the sequential velocity steps, winnowing some of the clay from the bed before the threshold was passed for the sand grains. Figure 8 clearly shows that for the wave-only and wave-current cases, the initiation time is related to the fraction of the wave cycle when shear stresses are above threshold. However, the current-only cases

are fundamentally different as a substantial initiation time infers that the bed *must* initially be below threshold. In Baas et al.'s (2013) experiments, the $C_0 = 16.2$ and 18% cases resulted in substantial initiation times (Table A2). Since the experiment with $C_0 = 13.8\%$ of Baas et al. (2013) did not have a substantial initiation time, it can be assumed to be above threshold. Taking the lowest θ_c for large ripples ($C_0 = 11.8\%$) to represent the limiting case ($\theta_{0E} = \theta_c$); this gives $P_\theta = 6.4$ in Equation 7, which is close to Whitehouse et al.'s (2000) accepted range and is then consistent with all Baas et al.'s (2013) current-only experiments.

The critical shear stress enhancement for all mixed sand–kaolinite experiments can therefore be expressed as

$$\theta_{0E} = \theta_0 \times \begin{cases} 1 + 6.4C_0, & D_{50} = 0.143 \text{ mm}, \\ 1 + 23C_0, & 0.45 \leq D_{50} \leq 0.50 \text{ mm}, \end{cases} \tag{9}$$

where $\theta_0 = 0.061$, for $D_{50} = 0.143$ mm, and $\theta_0 = 0.032$, for $0.45 \leq D_{50} \leq 0.5$ mm. Equation 9 states that there is a stronger enhancement of the threshold of motion for coarse sand compared to fine sand. This grain-size difference has been explained by van Rijn (2019) in terms of the clay content required to envelop a sand particle. Specifically, to completely envelop sand grains with a clay layer of thickness, d, the volumetric concentration of clay required can be expressed as an increasing function of d/D_{50}. Therefore, for a given clay concentration, the ratio of d around the two sand sizes is given by 0.45/0.143 ≈ 3. Interestingly, this ratio is similar to the ratio of constants in Equation 9 for the two grain sizes. Thus, the thicker clay layer around the coarser grains likely causes increased enhancement of the threshold of motion, which has also been found in field observations (Harris et al., 2016). It can be expected that the Baas et al. (2021) field data, where $D_{50} = 0.227$ mm and $0.6 \leq C_0 \leq 5.4\%$, should have a coefficient somewhere between 6.4 and 23. The coefficient would probably be closer to 6.4, as there was no obvious change in the threshold during the field campaign. However, it is difficult to be more specific as the dominant clay mineral in the sediment was illite rather than kaolinite and there is also the presence of extracellular polymeric substances (EPS) to consider (Malarkey et al., 2015; Baas et al., 2019).

4.4 Bedform phase diagrams

As proposed by Schindler et al. (2015), clay content can be incorporated into 3D phase diagrams. This has been done in Figure 9a and b by making use of Equation 9 and separating all the data depicted in Figure 2 into the two different grain-size ranges: $0.45 \leq D_{50} \leq 0.5$ mm and $D_{50} = 0.143$ mm (for the latter case only the current shear stress axis is shown as there is insufficient data for the full 3D plot). In this new 3D phase diagram framework, there are four main regions: no motion (NM), ripples (R), small ripples (SR), and washed-out ripples (WO). The upper boundary of NM is the yellow surface described by $\theta_w + \theta_c = \theta_{0E}$, where θ_{0E} is given by Equation 9, such that $\theta_{0E} = \theta_0$ when $C_0 = 0\%$. The NM region gradually expands with increasing C_0. This expanding region means the threshold eventually reaches the washout limit, $\theta_{0E} = \theta_{wo}$, where the ripple height starts to decrease near sheet flow conditions. Here, $\theta_{0E} = \theta_{wo}$ corresponds to $C_0 = 19.6\%$, for $0.45 \leq D_{50} \leq 0.5$ mm, and $C_0 = 30.9\%$, for $D_{50} = 0.143$ mm, which is broadly consistent with Whitehouse et al.'s (2000) lower limit of between 20 and 30% for cohesive erosion in mixtures of sand and clay.

In Figure 9a, the large and small ripple regions are each subdivided into three subregions: wave-dominant (W and SW; $\theta_c < 0.2\theta_w$), wave-current (WC and SWC; $0.2\theta_w < \theta_c < 3.3\theta_w$), and current-dominant (C and SC; $\theta_c > 3.3\theta_w$). The C/SC subdivision is shown in Figure 9b. Figure 9a also shows 2D cross-sections viewed from the $C_0 = 0\%$ end: (i) $0 \leq C_0 \leq 5.7\%$; (ii) $5.7 < C_0 \leq 10.6\%$; and (iii) $10.6 < C_0 \leq 19.6\%$, and marked in the 3D plot for reference. In Figure 9b for $D_{50} = 0.143$ mm, the small current ripples for $C_0 = 16.2\%$ and 18% appear in the NM region because it is thought that these cases were initially below threshold, as explained in Section 4.3. It is also likely that these ripples had not reached equilibrium (Table A2; Baas et al., 2013). This illustrates the point that this phase diagram is dynamic: even if the flow conditions place the data in the no movement region for sand, or indeed the washout region, clay can still be winnowed out of the bed as it was in some of the WC3 and WC2 cases (Figure 5f, g, h and k).
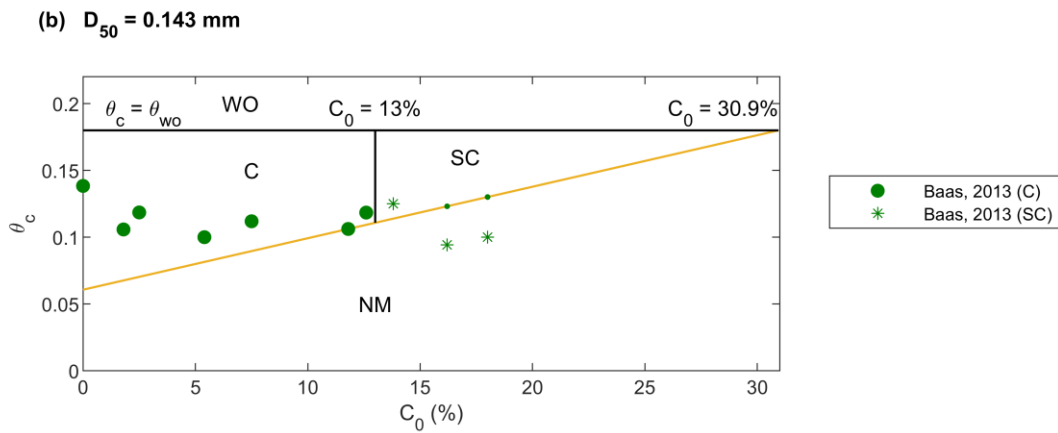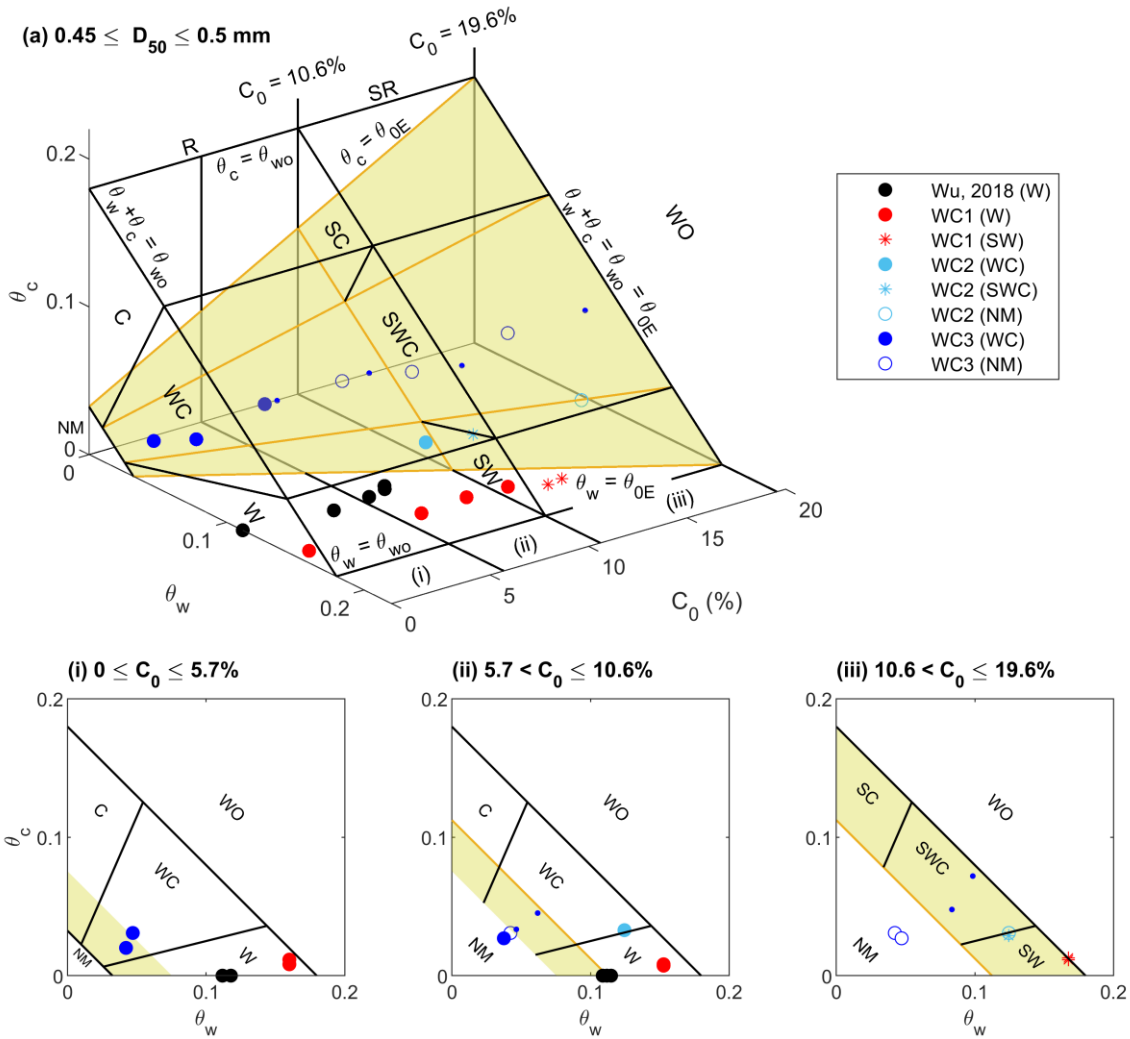
Figure 9. Orthographic projection of the 3D phase diagram with clay dependence for $0.45 \leq D_{50} \leq$ 0.50 mm (a) and 2D C_0-θ_c plot for $D_{50} = 0.143$ mm (b), with the enhance critical shear stress, θ_{0E}, based on Equation 9, represented as the yellow surface. Below threshold cases have appropriately coloured small dots to mark the critical shear stress on the surface. In (a) there are also three 2D cross-sections viewed from the $C_0 = 0\%$ end: (i) $0 \leq C_0 \leq 5.7\%$ (ii) $5.7 < C_0 \leq$ 10.6% and (iii) $10.6 < C_0 \leq 19.6\%$ and marked in the 3D plot. Solid circles: large ripples (R), asterisks: small ripples (SR), open circles: no ripples, C: current-dominant, WC: wave-current and W: wave-dominant (S prefix for small ripples), NM: no motion and WO: washout.

5 Implications for paleowave climate predictions and bedform phase diagrams

The reduction in ripple wavelength with increasing C_0, and specifically how it relates to the orbital diameter through Equation 6, may have consequences for paleoenvironmental reconstruction. Based on orbital ripples preserved in the rock record, Diem (1985) used $\alpha = 0.65$ to determine the orbital diameter and hence the palaeowave climate, which included water depth and wave height and period. Thus, it is likely that if α is lowered by the presence of clay this would underpredict the ancient orbital diameter, resulting in inaccurate paleowave climate predictions.

The predictions of the new 3D phase diagram framework show a dramatic reduction in bedform size and therefore form roughness, which is proportional to η^2/λ (Soulsby, 1997). In the specific case of Baas et al.'s (2021) intertidal field site in the Dee Estuary, on which the 2D phase diagram (Figure 2) is based, there were no instances of smaller flatter ripples, which is consistent with the range of C_0 measured: $0.6 \leq C_0 \leq 5.4\%$. However, considering the widespread occurrence of mixed sand and mud flats (Murray et al., 2019), the scenario that an increase in the threshold shear stress in the presence of clay significantly affects the state of the bed could occur frequently. Thus, it is likely that ripple dimensions could have been commonly overestimated by existing ripple predictors, potentially affecting the performance of morphodynamic models. The applicability of these 3D phase diagrams therefore requires further testing in muddy environments.

Conclusions

The present experiments examined ripple dynamics on cohesive beds under two different combined wave–current conditions with initial clay content, C_0, ranging from 0 to 18.3%. For the lowest C_0, these experiments produced quasi-asymmetric ripples, which are similar to their clean sand counterparts, with equilibrium heights and wavelengths in the range $13.9 \leq \eta_e \leq 15$ mm and $137 \leq \lambda_e \leq 148$ mm, respectively, with the larger values corresponding to the strongest relative current. For higher C_0, smaller, flatter ripples that were fully asymmetric, with $\eta_e = 5.6$ mm and $\lambda_e = 125$ mm, were produced. Finally, for the highest C_0, no ripples were produced and the bed remained flat.

Combining the present experiments with previous wave-only and wave-current experiments (Wu et al., 2018; 2022) demonstrates the existence of a large to small equilibrium ripple discontinuity at $C_0 = 10.6\%$, with two distinct ripple steepness (RS) groupings, RS ≥ 0.09 and RS ≈ 0.04, which is probably related to a three-orders of magnitude decrease in the hydraulic conductivity. The larger RS grouping shows a decrease from 0.14 to 0.1 with increasing current strength. Ripple wavelength was independent of initial clay content for $C_0 \leq 7.4\%$, but it decreased linearly with initial clay content for $C_0 > 7.4\%$. For $C_0 \leq 7.4\%$, the wavelength was proportional to the current-enhanced orbital diameter, d_{wc}, so that $\lambda_e = \alpha d_{wc}$, where $\alpha = 0.61$. For $C_0 > 7.4\%$, α decreased linearly, which could be important for paleoenvironment reconstruction, when λ_e is measured and d_{wc} is unknown. During the experiments, clay winnowing removed clay from both the active layer (crest to trough) and deep beneath it, in the case of most large ripples. Winnowing was quantified by the average mass flux of clay out of the bed over the duration of the experiment. Winnowing still occurred from flat beds, but compared to the large ripples the flux was typically two orders of magnitude smaller.

The ripple initiation time increased with initial clay content, and ultimately the bed remained flat when the initial clay content was large enough, demonstrating the enhancement of the threshold of sediment motion with increased initial clay content. When combined with the fine-sand, current-only experimental results of Baas et al. (2013), this allowed the enhancement of the threshold to be quantified for both coarse ($0.45 \leq D_{50} \leq 0.5$ mm) and fine ($D_{50} = 0.143$ mm) mixed sand–clay motion. On the basis of these enhancements, new 3D phase diagrams, involving the non-dimensional wave and current shear stresses

and C_0 are proposed to characterise the two ripple size groupings under different flow conditions. This

535   new 3D phase diagram framework should prove important to the morphodynamic modelling community.

Nomenclature

C	Measured core clay content		η_e	Equilibrium ripple height
C_0	Initial clay content		η_t	Mean ripple height at time t
C_{def}	Clay deficit ($= C_0{-}C$)		θ	Instantaneous Shields parameter
D_*	Dimensionless grain size		θ_0	Clean-sand threshold Shields parameter
D_{10}	10th percentile of sand		θ_{0E}	Enhanced threshold Shields parameter
D_{10m}	10th percentile of sand–clay mixture		θ_c	Current-only Shields parameter
D_{50}	Median grain size of sand		θ_{rms}	Root-mean-square of θ
D_{50c}	Median grain size of clay		θ_w	Wave-only Shields parameter
d_c	Equivalent clean-sand depth ($= I/C_0$)		θ_{wo}	Washout Shields parameter
d_{wc}	Current-enhanced orbital diameter		λ	Ripple wavelength
F_b	Average mass flux of clay out of bed		λ_e	Equilibrium ripple wavelength
g	Acceleration due to gravity		λ_l	Length of ripple lee side
H	Wave height		λ_s	Length of ripple stoss side
h	Water depth		λ_t	Mean ripple wavelength at time t
I	Total amount of clay removed from bed		v	Kinematic viscosity of water
T	Wave period		ρ	Water density
T_η	Equilibrium time for ripple height		ρ_s	Sediment density
T_λ	Equilibrium time for ripple wavelength		τ_c	Current-only skin friction
t	Bed scanning time		τ_w	Wave-only skin friction
t_d	Duration of experiment			
t_i	Time of first appearance of ripples			
U_c	Depth-average current velocity		**Abbreviations**	
U_w	Wave velocity amplitude		NM	No movement
u_*	Shear velocity scale		NR	No ripples
z	Vertical position relative to crest		RS	Ripple steepness ($= \eta_e/\lambda_e$)
α	Constant of proportionality		RSI	Ripple symmetry index ($= \lambda_s/\lambda_l$)
η	Ripple height		WO	washout

Appendices

Appendix A: Experimental conditions of Wu et al., (2022), Baas et al. (2013) and Wu et al. (2018).

Table A1. Wave-current experiments of Wu et al. (2022), where $h = 400$ mm, $T = 2$ s, $D_{50} = 0.45$ mm, $v = 1.12$ mm^{2}s^{-1} and $\rho = 1000$ kg m^{-3} and referred to in the main text as WC1 ($\theta_0 = 0.032$). Bedforms developed in all cases (R). *This fit is based on fitting two stages to the growth (see Wu et al., 2022)

C_0	U_w	U_c	θ_w	θ_c	η_e	T_η	λ_i	λ_e	T_λ	t_i
(%)	(mm/s)	(mm/s)	(-)	(-)	(mm)	(min)	(mm)	(mm)	(min)	(min)
0	320	160	0.160	0.008	14.4±1.8	90	80.7±10.8	123.6±4.9	170	0
5.7	320	190	0.160	0.012	14.7±1.1	125	91.3±6.3	126.5±3.5	330	5
8.5	310	160	0.153	0.008	14.3±1.0	432	80.2±11.6	121.4±5.1	456	60
10.6*	310	150	0.153	0.007	13.7±1.0	678	92.6±10.2	110.9±4.0	540	60
11.6	330	190	0.168	0.012	4.1±0.4	271	84.5±10.0	108.5±2.6	382	90
12.3	330	200	0.168	0.013	3.5±0.3	211	71.7±6.3	98.0±1.7	499	120

Table A2. Current-alone experiments of Baas et al. (2013), with $U_w = 0$ mm/s ($\theta_w = 0$), $D_{50} = 0.143$ mm, $v = 1.02$ mm^{2}s^{-1} and $\rho = 1000$ kg m^{-3} ($\theta_0 = 0.061$). Bedforms developed in all cases (R). *Equilibrium not reached after 2 h.

C_0	h	U_c	θ_c	η_e	T_η	λ_i	λ_e	T_λ	t_i
(%)	(mm/s)	(mm/s)	(-)	(mm)	(min)	(mm)	(mm)	(min)	(min)
0	248	400	0.138	16.2±0.5	64±8	28.5	116.3±3.5	81±16	0
1.8	250	350	0.106	13.6±0.8	53±10	46.1	95.5±3.9	83±20	3
2.5	247	370	0.118	14.1±0.8	40±8	40.2	115.3±5.6	69±19	5
5.4	248	340	0.100	13.3±0.8	74±12	35.7	98.4±8.2	87±34	5
7.5*	250	360	0.112	10.5±0.6	68±10	65.8	113.4±48.7	320±449	7
11.8	246	350	0.106	9.6±0.6	44±8	52.2	86.7±5.8	70±40	4
12.6	248	370	0.118	11.8±0.6	50±7	57.4	119.3±28.0	196±154	5
13.8	246	380	0.125	5.3±0.4			77.7±3.6		4
16.2	247	330	0.094	2.5±0.6			51.4±5.4		44
18.0	247	340	0.100	4.0±0.3			79.4±4.2		83

Table A3. Wave-alone experiments of Wu et al. (2018), with $U_c = 0$ mm/s ($\theta_c = 0$), $h = 600$ mm, $T = 2.48$ s, $D_{50} = 0.496$ mm, $v = 1.14$ mm^{2}s^{-1}, $\rho = 1015$ kg m^{-3} and $U_w = \frac{1}{2}(U_{won}+U_{woff}) \pm\frac{1}{2}(U_{won}-U_{woff})$, where U_{won} and U_{woff} are the onshore and offshore freestream velocities ($\theta_0 = 0.032$). Bedforms developed in all cases (R).

C_0	U_w	θ_w	η_e	T_η	λ_i	λ_e	T_λ	t_i
(%)	(mm/s)	(-)	(mm)	(min)	(mm)	(mm)	(min)	(min)
0	275±25	0.112	19.8±0.3	27±5	87.5±8.5	135.9±0.8	40±4	0
4.2	285±25	0.118	20.3±0.5	27±14	101.2±12.4	138.5±1.3	66±7	7
6.2	280±20	0.115	19.7±0.5	76±17	97.4±12.2	135.0±2.0	105± 32	42±17
7.2	275±15	0.112	20.3±0.7	120±38	109.1±8.8	139.2±3.0	184± 43	75±35
7.4	270±20	0.109	19.9±0.7	122±55	103.1±8.4	142.3±1.5	200± 68	62±34

Appendix B: Determining the effective orbital diameter under combined flow

For a colinear sinusoidal wave and current, the horizontal velocity close to the bed is

$$u_{wc} = U_w(\cos\varphi + b), \qquad \text{B1}$$

where $\varphi = \sigma t$ is the phase of the wave, $\sigma = 2\pi/T$, t is time, $b = AU_c/U_w$ and A is constant ($A < 1$ as the near-bed current will be less than the depth-averaged current velocity). Figure B1 shows Equation B1 graphically. The orbital diameter, which is the horizontal distance moved between the two flow reversals for the positive wave half cycle is shown by the shaded area under the curve. The zero-crossing phase is given by

$$\varphi_0 = \arccos[\max(-b, -1)]. \qquad \text{B2}$$

When $b \geq 1$, $\varphi_0 = \pi$; there are no zero crossings, and only a single minimum. The effective orbital diameter, d_{wc}, corresponding to the shaded area in Figure B1 is

$$d_{wc} = 2\sigma\int_0^{\varphi_0}u_{wc}d\varphi = d_0(\sin\varphi_0 + b\varphi_0), \qquad \text{B3}$$

where $d_0 = U_wT/\pi$ (Soulsby, 1997) is the orbital diameter for the wave alone, when $b = 0$. For the wave-current experiments, the value of A used in the parameter b was $A = 0.1$, 0.22 and 0.42 for WC1, WC2 and WC3, respectively, and for the wave-alone Wu et al. (2018) experiments $d_{wc} = d_0$ since $b = 0$.
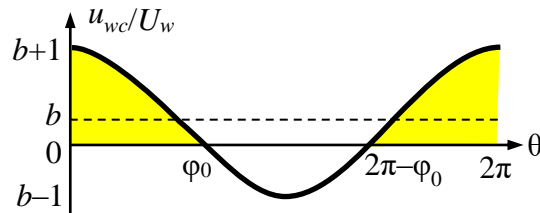
Figure B1. Plot of Equation B1, where shaded area represents d_{wc} in Equation B3.

Data availability

Supporting data are available through figshare which is a free and open repository (Wu et al., 2023).

Author contribution

XW and RF designed and carried out experiments. XW, JM, RF and EP processed experimental data. XW prepared the original manuscript. JM, JB, RF, and DP reviewed and edited the manuscript. DP acquired project funding and supervised the project.

Competing interests

DP is member of the editorial board of journal *Earth Surface Dynamics*. The peer-review process was guided by an independent editor, and the authors have also no other competing interests to declare.

Acknowledgments

The authors acknowledge the enormous contributions of Brendan Murphy, whose help throughout the study made our setup, data collection, and clean-up efforts smooth and trouble free. The authors acknowledge Oliver Dawes and the Hull Marine Laboratory at the University of Hull for their support in processing grain sizes with the Malvern Mastersizer 2000. Participation of XW, JM, RF, JHB, EP and DRP was made possible thanks to funding by the European Research Council under the European Union's Horizon 2020 research and innovation program (grant no. 725955). Participation of RF was also

supported by the Leverhulme Trust and Leverhulme Early Career Researcher Fellowship (grant ECF-2020-679).

References

585   Arnott, R. W. & Southard, J. B. 1990. Exploratory flow-duct experiments on combined-flow bed configurations, and some implications for interpreting storm-event stratification. *Journal of Sedimentary Research,* 60, 211-219.

Baas, J. H., Baker, M. L., Malarkey, J. Bass, S. J., Manning, A. J., Hope, J. A., Peakall, J., Lichtman, I. D., Ye, L., Davies, A. G., Parsons, D. R., Paterson, D. M. & Thorne, P. D. 2019. Integrating field 590   and laboratory approaches for ripple development in mixed sand–clay–EPS. *Sedimentology,* 66, 2749-2768.

Baas, J., Malarkey, J, Lichtman, I. D., Amoudry, L. O., Thorne, P., Hope, J. A., Peakall, J., Paterson, D. M., Bass, S. & Cooke, R. D. 2021. Current-and Wave-Generated Bedforms on Mixed Sand–Clay Intertidal Flats: A New Bedform Phase Diagram and Implications for Bed Roughness and 595   Preservation Potential. *Frontiers Earth Science,* 9, 747567.

Baas, J. H., Davies, A. G. & Malarkey, J. 2013. Bedform development in mixed sand–mud: The contrasting role of cohesive forces in flow and bed. *Geomorphology,* 182, 19-32.

Bartzke, G., Bryan, K. R., Pilditch, C. A. & Huhn, K. 2013. On the stabilizing influence of silt on sand beds. *Journal of Sedimentary Research,* 83, 691-703.

600   Beard, J. A., Bush, A. M., Fernandes, A. M., Getty, P. R. & Hren, M. T. 2017. Stratigraphy and paleoenvironmental analysis of the Frasnian-Famennian (Upper Devonian) boundary interval in Tioga, north-central Pennsylvania. *Palaeogeography, Palaeoclimatology, Palaeoecology,* 478, 67-79.

Brakenhoff, L., Schrijvershof, R., van der Werf, J., Grasmeijer, B., Ruessink, G. & van der Vegt, M. 2020. 605   From ripples to large-scale sand transport: The effects of bedform-related roughness on hydrodynamics and sediment transport patterns in delft3d. *Journal of Marine Science and Engineering,* 8, 892.

Chapuis, R. P. 2012. Predicting the saturated hydraulic conductivity of soils: a review. *Bulletin of Engineering Geology and the Environment*, 71, 401-434.

Clifton, H. E. & Dingler, J. R. 1984. Wave-formed structures and paleoenvironmental reconstruction. *Marine Geology*, 60, 165-198.

Cummings, D. I., Dumas, S. & Dalrymple, R. W. 2009. Fine-grained versus coarse-grained wave ripples generated experimentally under large-scale oscillatory flow. *Journal of Sedimentary Research,* 79, 83-93.

Diem, B. 1985. Analytical method for estimating palaeowave climate and water depth from wave ripple marks. *Sedimentology,* 32, 705-720.

Dumas, S., Arnott, R. & Southard, J. B. 2005. Experiments on oscillatory-flow and combined-flow bed forms: implications for interpreting parts of the shallow-marine sedimentary record. *Journal of Sedimentary research,* 75, 501-513.

Gao, S. 2019. Geomorphology and sedimentology of tidal flats. *Coastal Wetlands.* Elsevier.

Harris, R. J., Pilditch, C. A., Greenfield, B. L., Moon, V. & Kröncke, I. 2016. The influence of benthic macrofauna on the erodibility of intertidal sediments with varying mud content in three New Zealand estuaries. *Estuaries and Coasts,* 39, 815-828.

Healy, T., Wang, Y. & Healy, J.-A. 2002. *Muddy coasts of the world: processes, deposits and function*, Elsevier.

Héquette, A., Hemdane, Y. & Anthony, E. J. 2008. Sediment transport under wave and current combined flows on a tide-dominated shoreface, northern coast of France. *Marine geology,* 249, 226-242.

Higashino, M., Clark, J. J. & Stefan, H. G. 2009. Pore water flow due to near‐bed turbulence and associated solute transfer in a stream or lake sediment bed. *Water resources research,* 45(12), W12414, doi: 10.1029/2008WR007374.

Huettel, M., Ziebis, W. & Forster, S. 1996. Flow‐induced uptake of particulate matter in permeable sediments. *Limnology and Oceanography,* 41(2), 309-322.

Jiang, Q., Liu, D., Jin, G., Tang, H., Wei, Q. & Xu, J. 2022. N_2O dynamics in the hyporheic zone due to ripple migration. *Journal of Hydrology,* 610, 127891.

635   Khelifa, A. & Ouellet, Y. 2000. Prediction of sand ripple geometry under waves and currents. *Journal of waterway, port, coastal, and ocean engineering,* 126, 14-22.

Kleinhans, M. 2005. Phase diagrams of bed states in steady, unsteady, oscillatory and mixed flows. In *SANDPIT, Sand Transport and Morphology of Offshore Sand Mining Pits*, L. C. van Rijn, R. L. Soulsby, P. Hoekstra and A. G. Davies (editors), Aqua Publications, Amsterdam, Paper Q.

640   Li, M. Z. & Amos, C. L. 1999. Field observations of bedforms and sediment transport thresholds of fine sand under combined waves and currents. *Marine Geology,* 158, 147-160.

Malarkey, J., Baas, J. H., Hope, J. A., Aspden, R. J., Parsons, D. R., Peakall, J., Paterson, D. M., Schindler, R. J., Ye, L. & Lichtman, I. D. 2015. The pervasive role of biological cohesion in bedform development. *Nature communications,* 6, 6257, doi: 10.1038/ncomms7257.

645   Malarkey, J. & Davies, A. G. 2012. A simple procedure for calculating the mean and maximum bed stress under wave and current conditions for rough turbulent flow based on method. *Computers & Geosciences,* 43, 101-107.

Mousavi, M. E., Irish, J. L., Frey, A. E., Olivera, F. & Edge, B. L. 2011. Global warming and hurricanes: the potential impact of hurricane intensification and sea level rise on coastal flooding. *Climatic*
650   *Change,* 104, 575-597.

Murray, N.J., Phinn, S.R., DeWitt, M., Ferrari, R., Johnston, R., Lyons, M. B., Clinton, N., Thau, D. and Fuller, R. A. 2019. The global distribution and trajectory of tidal flats. *Nature*, 565, 222-225.

Myrow, P., Snell, K., Hughes, N., Paulsen, T., Heim, N. & Parcha, S. 2006. Cambrian depositional history of the Zanskar Valley region of the Indian Himalaya: tectonic implications. *Journal of*
655   *Sedimentary Research,* 76, 364-381.

Osborne, P. D. & Greenwood, B. 1993. Sediment suspension under waves and currents: time scales and vertical structure. *Sedimentology,* 40, 599-622.

Packman, A.I., Salehin, M. & Zaramella, M., 2004. Hyporheic exchange with gravel beds: Basic hydrodynamic interactions and bedform-induced advective flows. *Journal of Hydraulic*
660   *Engineering*, 130(7), 647-656.

Pedocchi, F. & García, M. 2009. Ripple morphology under oscillatory flow: 2. Experiments. *Journal of Geophysical Research: Oceans,* 114, C12015, doi:10.1029/2009JC005356.

Perillo, M. M., Best, J. L. & Garcia, M. H. 2014. A new phase diagram for combined-flow bedforms. *Journal of Sedimentary Research,* 84, 301-313.

665 Perron, J. T., Myrow, P. M., Huppert, K. L., Koss, A. R. & Wickert, A. D. 2018. Ancient record of changing flows from wave ripple defects. *Geology,* 46, 875-878.

Precht, E. & Huettel, M. 2003. Advective pore‑water exchange driven by surface gravity waves and its ecological implications. *Limnology and Oceanography,* 48, 1674-1684.

Rogers, C., Dijkstra, T. & Smalley, I. 1994. Particle packing from an Earth science viewpoint. *Earth-*
670 *Science Reviews,* 36, 59-82.

Schindler, R. J., Parsons, D. R., Ye, L., Hope, J. A., Baas, J. H., Peakall, J., Manning, A. J., Aspden, R. J., Malarkey, J., Simmons, S., Patterson, D. M., Lichtman, I. D., Davies, A. G., Thorne P. D. & Bass, S. J. 2015. Sticky stuff: redefining bedform prediction in modern and ancient environments. *Geology*, 43, 399-402.

675 Sleath, J. F. A., 1984. *Seabed Mechanics*. Wiley.

Soulsby, R. 1997. *Dynamics of Marine Sands: A manual for pratical applications*. Thomas Telford.

Sumer, B. M., Whitehouse, R. J. & Tørum, A. 2001. Scour around coastal structures: a summary of recent research. *Coastal Engineering,* 44, 153-190.

Tanaka, H. & Dang, V. T. 1996. Geometry of sand ripples due to combined wave-current flows. *Journal*
680 *of waterway, port, coastal, and ocean engineering,* 122, 298-300.

Teitelbaum, Y., Dallmann, J., Phillips, C. B., Packman, A. I., Schumer, R., Sund, N. L., Hansen, S. K. & Arnon, S. 2021. Dynamics of hyporheic exchange flux and fine particle deposition under moving bedforms. *Water Resources Research*, 57(4), p.e2020WR028541.

Teitelbaum, Y., Shimony, T., Saavedra Cifuentes, E., Dallmann, J., Phillips, C.B., Packman, A.I., Hansen,
685 S.K. and Arnon, S., 2022. A novel framework for simulating particle deposition with moving bedforms. *Geophysical Research Letters*, 49(4), p.e2021GL097223.

van den Berg, J. & van Gelder, A. 1993. A new bedform stability diagram, with emphasis on the transition of ripples to plane bed in flows over fine sand and silt. *Special Publications of the International Association of Sedimentologists,* 17, 11-21.

690 van Rijn, L.C., 2019. Erodibility of Mud-Sand Bed Mixtures. *Journal of Hydraulic Engineering,* 146(1), 04019050.

Vercruysse, K., Grabowski, R. C. & Rickson, R. 2017. Suspended sediment transport dynamics in rivers: Multi-scale drivers of temporal variation. *Earth-Science Reviews,* 166, 38-52.

Vitousek, S., Barnard, P. L., Fletcher, C. H., Frazer, N., Erikson, L. & Storlazzi, C. D. 2017. Doubling of 695 coastal flooding frequency within decades due to sea-level rise. *Scientific reports,* 7, 1-9.

Whitehouse, R., Soulsby, R., Roberts, W. & Mitchener, H. 2000. *Dynamics of Estuarine Muds: A Manual for Practical Applications*, Thomas Telford.

Wiberg, P. L. & Harris, C. K. 1994. Ripple geometry in wave‐dominated environments. *Journal of Geophysical Research: Oceans,* 99, 775-789.

700 Wu, X., Baas, J. H., Parsons, D. R., Eggenhuisen, J., Amoudry, L., Cartigny, M., Mclelland, S., Mouazé, D. & Ruessink, G. 2018. Wave Ripple Development on Mixed Clay‐Sand Substrates: Effects of Clay Winnowing and Armoring. *Journal of Geophysical Research: Earth Surface,* 123, 2784-2801.

Wu, X., Fernández, R., Baas, J. H., Malarkey, J. & Parsons, D. R. 2022. Discontinuity in equilibrium 705 wave-current ripple size and shape and deep cleaning associated with cohesive sand-clay beds. *Journal of Geophysical Research Earth Surface*, 127, e2022JF006771.

Wu, X., Malarkey, J., Fernandez, R., Baas, J. H. & Parsons, D. R. 2023. Flume experiments to investigate the influence of cohesive clay on wave-current ripple dynamcis. figshare. Dataset. https://doi.org/10.6084/m9.figshare.22578529.v1

710 Yokokawa, M. 1995. Combined-flow ripples: genetic experiments and applications for geologic records. *Series D, Earth and planetary sciences*. 29 (1), 1-38, 1995-12-26, Faculty of Science, Kyushu University.